

The Australian Coastal Experiment: A Search for Coastal-Trapped Waves^{||}

H. J. FREELAND*, F. M. BOLAND, J. A. CHURCH, A. J. CLARKE**, A. M. G. FORBES, A. HUYER[‡],
R. L. SMITH[‡], R. O. R. Y. THOMPSON[®] AND N. J. WHITE

CSIRO Division of Oceanography, Hobart, Tasmania, 7001, Australia

(Manuscript received 8 July 1985, in final form 13 January 1986)

ABSTRACT

The Australian Coastal Experiment (ACE) was conducted in the coastal waters of New South Wales from September 1983 to March 1984. The data obtained allow a detailed examination of the dynamics of flow on the continental shelf and slope and in particular allow a description of coastal trapped wave modes propagating within the coastal waveguide.

The trapped-wave signal is contaminated by energy from the East Australia current eddies approaching the continental slope. However, the data do allow a clear separation of the first three coastal trapped wave modes over the range of frequencies appropriate to the weather forcing band. Through that frequency range the phase speed is computed and an empirical dispersion relation determined for each mode. The empirical dispersion relations compare well with the theoretical relations indicating that a large fraction of the variance in current velocities on the continental shelf can be accounted for by coastal trapped wave theory.

Wind forcing of trapped waves is also considered and evidence presented that in the ACE area the motions are dominated by the propagation of free waves through the arrays.

1. Introduction

Hamon (1962, 1966) showed that the low-frequency part of sea-level variations along the eastern coast of Australia was substantially nonisostatic. Furthermore, the adjusted sea-level time series at different sites (adjusted to remove the isostatic response to atmospheric pressure fluctuations) showed a definite tendency to propagate phase northwards. Robinson (1964) suggested that the nonisostatic part of sea-level and its propagation northwards were due to the existence of a type of barotropic topographic Rossby wave trapped in a continental shelf and slope waveguide. Adams and Buchwald (1969) showed that the wind stress, rather than atmospheric pressure, was the dominant generator of shelf waves; Gill and Schumann (1974) showed that the pressure amplitude of each long shelf-wave mode satisfied a simple forced, first-order wave equation. Clarke (1977) showed that this latter result was applicable not only to barotropic continental shelf waves (CSWs) which depend only on the topography but also to the generalized type of wave motion, including the

effects of stratification, known as "coastal trapped waves" (CTWs).

It was shown by Brink and Allen (1978) and Brink (1982) that the forced first-order wave equations for the infinite set of wave modes are coupled by friction. Recently, Clarke and Van Gorder (1986) reexamined the frictional long-wave problem and suggested a means for calculating the response of a coastal oceanic region to a general wind-stress field.

A review article by Mysak (1980) listed numerous observations of sea-level and longshore current perturbations which show apparent pattern propagation speeds roughly compatible with the speeds predicted by CTW theory. Details aside, it does appear that current fluctuations do occur on most of the continental shelves of the world which can be interpreted to be some sort of topographic Rossby wave. CTWs have been ascribed an important role in causing or suppressing upwelling (Crépon and Richez, 1983) and with widespread effects on fisheries and weather (O'Brien et al., 1981). Despite their reputed importance, there has been little systematic field effort to verify that the dynamics of the perturbations are those appropriate to forced coastal trapped wave theory. All of the previous experimental studies of CTWs have had to use data collected primarily to study other phenomena such as tides or upwelling. Because of this Mysak (1980) wrote that "there is a pressing need for a CSW-designed field experiment, which has never been carried out in the past." It was specifically to respond to this "pressing need" that the Australian Coastal Experiment, or ACE,

^{||} The paper was compiled by the first author with contributions from the co-authors. The co-authors are listed in alphabetical order.

* Institute of Ocean Sciences, Sidney, B.C. V8L 4B2, Canada.

** Dept. of Oceanography, Florida State University, Tallahassee, FL 32306.

[‡] College of Oceanography, Oregon State University, Corvallis, OR 97331.

[®] P.O. Box 24, Lindisfarne, Tasmania 7015, Australia.

was designed and carried out off the coast of New South Wales (eastern Australia) between Cape Howe and Newcastle (see Fig. 1) during the period September 1983 to March 1984.

To carry out this experiment we needed a coast that 1) was accessible, 2) had fluctuations in sea level and velocity at a detectable level, 3) was free of complicating and obfuscating factors such as fronts, large topographic changes or rapid changes in stratification, and 4) was long enough for propagation to be evident. The experiment should not be carried out in a region dominated by large mean flows, so that the evolution of waves can be linear, and it was considered desirable that waves be at least partially generated within the study area. With these limitations and constraints, the New South Wales coast seemed to be a reasonable candidate.

A unique aspect of this experiment is that prior to the recovery of the experimental array, a paper was published by Clarke and Thompson (1984) that made specific predictions about the behavior of currents in

the ACE area. The predictions were based on a frictionless theory which we will summarize here.

The usual quasi-geostrophic equations of motion for a stratified Boussinesq ocean are written down and separable solutions sought of the form

$$p(x, y, z, t) = \sum_{n=1}^{\infty} F_n(x, z)\phi_n(y, t). \quad (1)$$

The functions $F_n(x, z)$ are the CTW eigenfunctions, depend on the offshore coordinate (x) and depth (z), and are solutions of an eigenvalue problem

$$F_{xx} + \left(\frac{f^2}{N^2} F_z\right)_z = 0 \quad (2)$$

with appropriate boundary conditions. In (2) N and f are the Brunt-Väisälä frequency and the Coriolis parameter, respectively. The eigenvalues for this problem are the long-wave phase speeds and emerge through the boundary conditions.

The functions $\phi_n(y, t)$ which describe the longshore evolution of the coastal trapped waves and the time variability satisfy a forced first-order wave equation

$$-\frac{1}{c_n} \frac{\partial \phi_n}{\partial t} + \frac{\partial \phi_n}{\partial y} = B_n \tau(y, t) \quad (3)$$

where c_n are the eigenvalues of the equation for $F_n(x, z)$, y is the longshore coordinate, τ is the longshore component of wind-stress, and the numbers B_n are coupling coefficients between the wind-stress and the modal eigenfunctions F_n . Using Eq. (3) the longshore evolution of currents in a coastal waveguide can be described if the initial current distribution can be expanded in a sum using the eigenfunctions F_n .

This is in principle a straightforward operation. If we write the longshore component of velocity at a particular line of moorings as $v(x, y, z, t)$ then we can expand velocities as

$$v(x, y, z, t) = \sum_{i=1}^{\infty} G_i(x, z)\phi_i(y, t) \quad (4)$$

and derive the relationship between $F_i(x, z)$ and $G_i(x, z)$ as

$$G_i(x, z) = \frac{1}{f} \frac{\partial F_i}{\partial x}. \quad (5)$$

For the ACE region, Clarke and Thompson noted that the observations of Hamon (1966) suggest the condition $\phi_n(0, t) = 0$, since he found sea-level to be nearly isostatic at Eden (see Fig. 1). This suggested that the ACE area would be dominated by the forced CTW, i.e., that signals should largely be generated within the experimental region by local wind stress, and the free CTWs that enter the southern end of the array should contribute little to the overall signal variance. Clarke and Thompson (1984) proposed various simple models for the distribution of wind stress and were able to

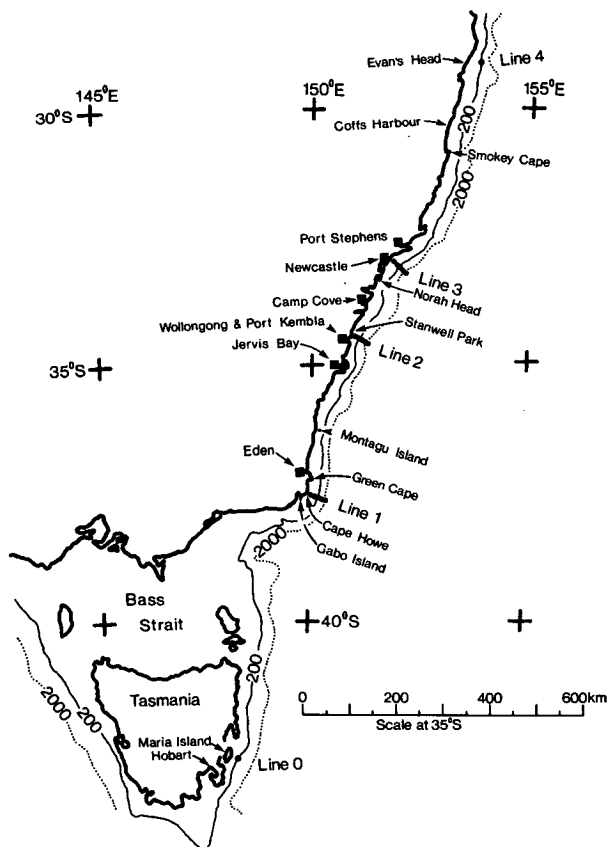


FIG. 1. Map of southeastern Australia showing the general area of the Australian Coastal Experiment, the principal landmarks referred to in the text, and a few depth contours. Tide gauge locations are marked by the symbol ■ and current meter moorings by the symbol ●.

make specific predictions about the behavior of currents:

1) Outside the surface and bottom Ekman layers, the low-frequency fluctuating wind-driven currents should be nearly alongshore and satisfy $v = (1/\rho_0) p_x / f$.

2) The alongshore current amplitude should decrease monotonically from the coast. For 1 dyn cm^{-2} longshore wind-stress amplitude, typical longshore current amplitudes at lines 2 and 3 (see Fig. 1) should be $10\text{--}20 \text{ cm s}^{-1}$. Significant longshore current amplitudes should be confined to the shelf and upper slope.

3) Longshore currents and adjusted sea levels should propagate northward along the coast at $4\text{--}5 \text{ m s}^{-1}$. Upward phase propagation should also be observed.

4) For the lower frequencies of the "weather" frequency band ($2\pi/\text{few days}$ – $2\pi/\text{few weeks}$) longshore current and adjusted sea-level amplitudes should increase northward from line 1 ($y = 0$).

5) The wind-driven current and sea-level fluctuations should be small at the Cape Howe, or line 1, section. This prediction results from an analysis of Hamon's (1966) data.

In this paper we will attempt a synthesis of the principal results from ACE that pertain to the propagation of coastal trapped waves. In doing this we will also draw on some results from more specific papers by Church et al. (1986), Church et al. (personal communication, 1986) and Forbes (personal communication, 1985).

In section 2 of this paper we will describe the deployment of equipment in the ACE experimental array, and comment on the data return and instrument failures. In section 3 we will describe some elementary observations of the general behavior of the current fluctuations, and we will empirically establish the likelihood of free waves. In section 4 we will decompose the current fluctuations into three coastal-trapped wave modes and 1 eddy mode at each of the three principal lines of moorings. The evolution of the modes from one line to another will allow us to compute empirical dispersion relations for the dynamical modes. In the final section we will discuss the implications of the previous analysis regarding the predictability of coastal current systems and discuss the possible origins of the energy fluxes observed.

2. The experiment

ACE was conducted off the east coast of New South Wales (Figs. 1, 2) for a six-month period between September 1983 and March 1984. The experiment included an array of current meters with three main lines with five moorings each, repeated CTD and XBT surveys, meteorological measurements from moored buoys and coastal stations, sea level measurements at coastal tide gauges, and bottom pressure measurements at a few sites. Several other types of data were also acquired as part of ACE but none of these will be explicitly discussed in this paper: satellite infrared images

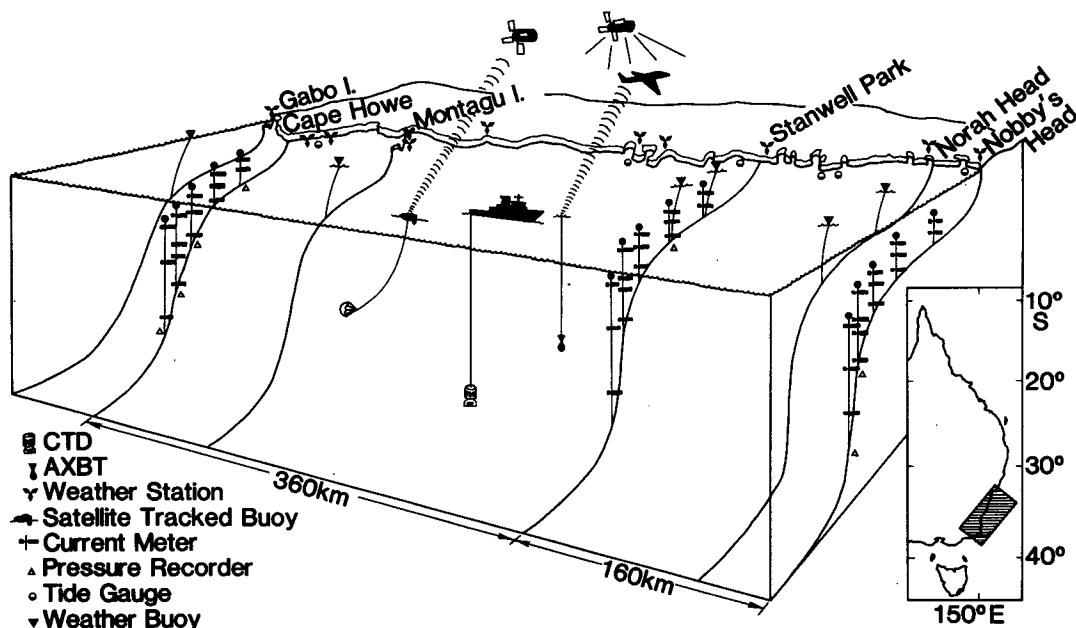


FIG. 2. A perspective view of the instrument array deployed in the intensive ACE area along the New South Wales coastline.

for determining the location of East Australia Current (EAC) eddies and meanders; AXBT profiles acquired by the Royal Australian Air Force; and satellite-tracked drifter buoys drogued at 200 m that were seeded into the EAC eddies and used to keep track of their movement (Wells and Cresswell, 1985).

a. The moored array

The current meter array consisted of three lines of moorings (Figs. 1 and 2) off Cape Howe in the south (line 1), Stanwell Park near Sydney (line 2), and Newcastle in the north (line 3). Two additional moorings were deployed, one off Evan's Head near Coff's Harbour at 29°S (line 4) and one off Maria Island off the east coast of Tasmania at 42°S (line 0). Each of the three principal lines was arranged perpendicular to the local coastline, was nominally identical with each other, and consisted of 15 Aanderaa current meters on 5 moorings (Table 1). Some of the moorings also carried Applied Microsystems tide gauges. Since we will want to refer to specific moorings in the array we have adopted a simple code: a mooring referred to as 23 will be on Line 2, and be the third mooring out from the coast. We identify individual current meters by adding a slash to the mooring designation and appending the depth of the specific current meter, e.g., 34/1000 is the current meter at 1000 m depth on Line 3, fourth mooring from the coast. A prefix letter "f" indicates a time series that has been low-pass filtered (<0.6 cpd) to remove tides and other high frequency signals, and the inclusion of the letter "p" indicates a bottom pressure record, e.g., fp11 is the low-pass filtered pressure record from the bottom of mooring 11.

Data from the current meter array have been summarized by Freeland et al. (1985). The current meter arrays returned about 70% of total possible data. Some moorings were lost due to commercial fishing and others from unexpectedly large currents (a meander in the EAC) hitting the northern line of moorings late in the experiment. These large currents (with a maximum speed of 168 cm s^{-1} at current meter 34/450) caused large vertical excursions of the tops of two moorings and caused four steel-sphere buoys to implode. Backup buoyancy farther down ensured that some useful data

TABLE 1. The depths of current meters and total water depths for the nominal arrays deployed on lines 1, 2 and 3. For lines 0 and 4 only mooring number 2 was deployed.

Mooring	Water depth (m)	Instrument depths (m)
1	140	75, 125
2	200	75, 125, 190
3	500	125, 190, 450
4	1200	190, 450, 650, 1000
5	2000	450, 1000, 1900

were recorded from these moorings even after the implosions.

b. CTD surveys

A total of 602 CTD stations were completed on six different cruises, one each month from September 1983 through February 1984 (data report in preparation). Most of these were acquired along the principal mooring lines and have been used in this paper to define the Brunt-Väisälä frequency profile in order to compute local shapes of the CTW eigenfunctions from Eq. (2). The CTD surveys were also used to keep track of the positions of the EAC eddies which had been known to occur in this region (Nilsson and Cresswell, 1981). The CTD surveys showed that eddies occurred very near the continental slope in late September and again in January and February. The eddies are interesting in their own right and will be described elsewhere, but in this paper they are treated as an undesirable source of noise.

c. Meteorological data

A number of Metspar meteorological buoys were deployed to measure the oceanic wind field, but for a variety of reasons the buoys did not report large amounts of data. Good quality wind data were obtained from a number of shore-based meteorological stations by the Australian Bureau of Meteorology. Some of these stations show evidence of topographic steering and could not be considered to represent the marine wind field; however, other stations compared well with the short time-series obtained from the Metspar buoys (Forbes, 1985). Figure 3 shows the time series of filtered alongshore wind speed measured at two Metspar buoys and at the shore-based stations closest to these stations. The Metspar time series are shown dotted overlaying the shore-based time series; the time series are clearly well correlated. The speed series correlate at $r = 0.76$ and 0.75 at Stanwell Park and Norah Head, respectively. Similar time series for wind stress yield correlations of 0.67 and 0.66. On the basis of this comparison, we decided to use data from seven shore-based wind stations: Gabo Island, Green Cape, Montagu Island, Wollongong (Port Kembla), Norah Head, Smokey Cape and Coff's Harbour (Fig. 1).

d. Bottom pressure and coastal sea level data

Bottom pressure was measured on Line 1 using Applied Microsystems pressure gauges moored on the bottom near moorings 11 and 13; both returned 100% data of excellent quality. Another bottom pressure gauge was moored at the bottom of mooring 31, but the data from this gauge may have been contaminated by mooring motion. Sea level data from coastal tide gauges at Eden, Jervis Bay, Port Kembla, Camp Cove in Sydney Harbour and Port Stephens (Fig. 1) were

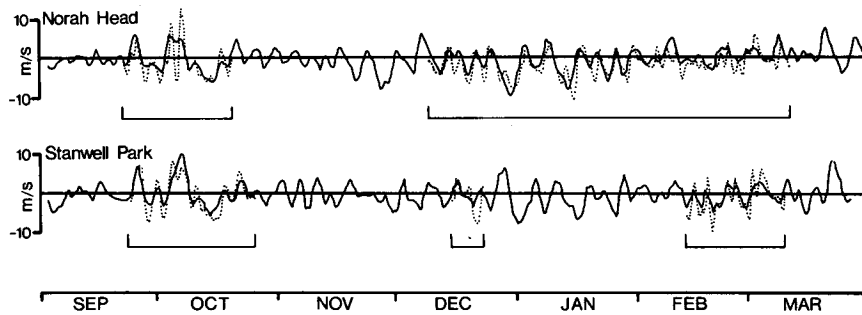


FIG. 3. The longshore component of wind speed measured at two METDATA buoys (dotted lines) plotted against time and superimposed on equivalent plots from nearby coastal wind stations.

obtained from the Maritime Services Board, Public Works Department of New South Wales. These data were adjusted for the “inverted barometer effect” using atmospheric pressure observations from nearby meteorological stations. A data report on the total pressure measurement array is in preparation.

3. Results

a. The velocity field

In Fig. 4 we show plots of current velocity vectors at two sites on each of the three principal lines and one series from the Maria Island, line 0, mooring. It is clear that there is some similarity among longshore current components between adjacent lines, particularly at the inshore locations. The currents between adjacent lines show greatest similarity when the more southerly currents are lagged somewhat in time. This implies northward propagation of current signals as expected.

The inshore currents shown on Fig. 4 clearly show considerable energy at periods appropriate to weather forcing. The same signals are also visible in the currents at sites offshore, but there is a distinct bias towards lower frequencies at those sites. This is probably due to the presence of EAC eddies in the ACE region.

Rather more startling are the general energy levels. The expectation of much lower energy levels at line 1, compared with the other two lines, is not supported by the observations. Also, though the energy levels offshore are lower than those over the shelf, the difference is not impressive; clearly there are signals in these time series besides the CTW activity.

For each current meter site the longshore component of velocity was Fourier transformed in 25 day blocks. In Fig. 5 we have contoured the variance along each line in the (x, z ; on-offshore and depth) plane for three periods, 25, 12½ and 6¼ days. In the magnitude of the variances, the three lines are remarkably similar, except for line 3 at a period of 25 days. In that case line 3 appears to have very much more energy than either of the other two lines. Only for two of the nine plots shown in the prediction, number 2, of Clarke and Thompson (1984) satisfied, that amplitudes should decrease

monotonically from inshore to offshore. Prediction 5, that wind-driven currents be small at line 1 fares no better; at a period of 6¼ days the distribution of variance, and actual magnitudes, are extremely similar at lines 1 and 3, and variances are substantially lower at line 2. The most notable difference between lines 1 and

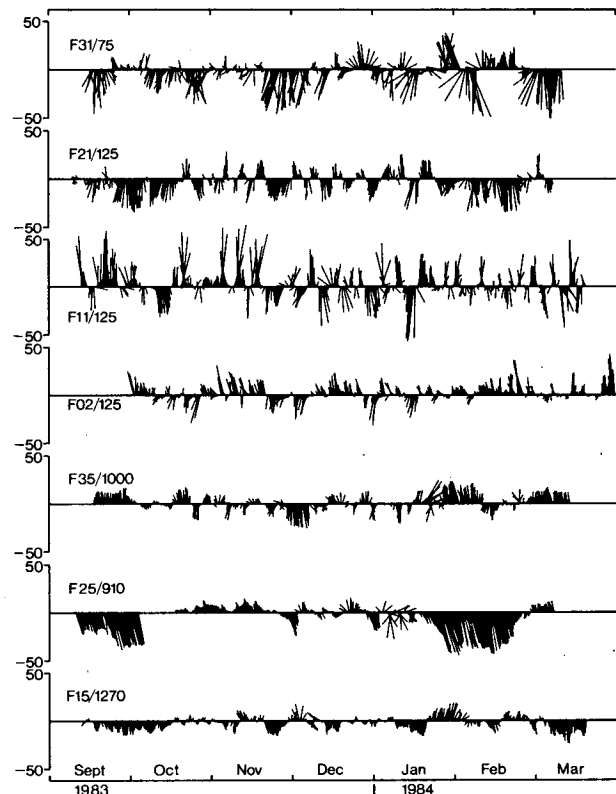


FIG. 4. Current vectors measured at two locations on each of the three principal lines of moorings, one site shallow and one site deep and one from the single mooring off Maria Island. The currents have been low-pass filtered using a Lanczos cosine filter having a half-power point of 40 h and subsampled at 12 h intervals. The currents plotted here are rotated so that the principal axis of variance is directed up and down the page. Very closely this corresponds to the longshore direction, with the direction NNE up the page.

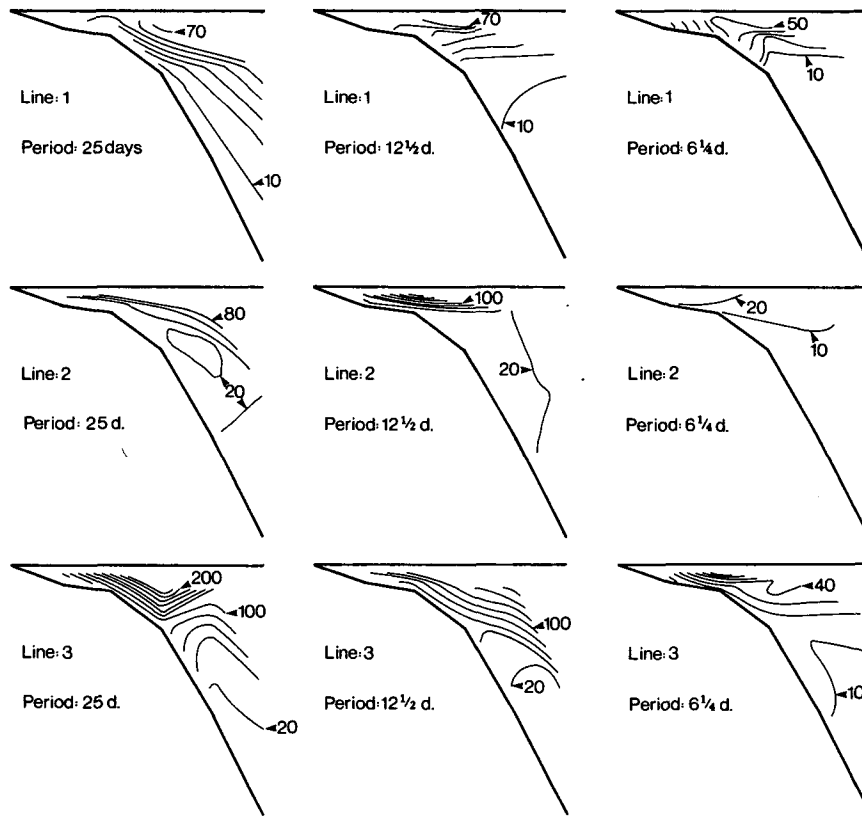


FIG. 5. Variance distribution along each of the three principal mooring lines at three frequencies in $(\text{cm s}^{-1})^2$.

3 at 6¼ days is the shift of the position of maximum variance from close inshore at line 1 to the shelf edge at line 3. At periods of 12½ days and 25 days the general pattern of variance distribution is very similar at each of the three lines, magnitudes are similar at lines 1 and 2, but substantially greater at line 3. Clearly, compared with the other two lines, it is not at all obvious that line 1 is quiescent and it appears that we must reject this prediction of Clarke and Thompson also.

b. Sea-level observations

We consider the sea level and bottom pressure observations from two points of view: 1) Are they consistent with Clarke and Thompson's prediction 5 and Hamon's (1966) sea level data? 2) Is there evidence of northward propagation in the subsurface pressure (adjusted sea level) signal?

Clarke and Thompson based their prediction 5 (that wind-driven sea level and current fluctuations should be small at Line 1) on "the analysis by Hamon (1966) that sea levels at Hobart are isostatic and at Eden very nearly so" (Clarke and Thompson, 1984, p. 340). Correlation and regression coefficients between pairs of ACE sea level and atmospheric pressure observations (Table 2) are in substantial agreement with Hamon's

where both exist, except that the ACE regression coefficients have much larger error bars. This difference arises because we estimate the integral time scale (Lumley and Panofsky, 1964) to be about 5 days (see Fig. 6), while Hamon apparently assumed each daily value represented an independent sample, i.e., Hamon overestimated the number of degrees of freedom by as much as a factor of five, and hence significantly underestimated his errors. It appears then that the ACE sea level data are in substantial agreement with Hamon's, yet the ACE current measurements contra-

TABLE 2. Sea level adjustment statistics. Correlation and regression coefficients between measured sea-level and local atmospheric pressure. Error bars are 95% confidence intervals.

Site	Regression coefficient (cm/mb)	Correlation coefficient	Duration of data (days)
fp11	-1.03 ± 0.31	-0.74	189½
Eden	-1.29 ± 0.43	-0.70	205
Jervis Bay	-0.58 ± 0.51	-0.42	143
Port Kembla	-0.35 ± 0.83	-0.18	119
Camp Cove	-0.65 ± 0.48	-0.40	204½
fp31	-1.02 ± 0.67	-0.47	176
Port Stephens	-0.61 ± 0.50	-0.37	204½

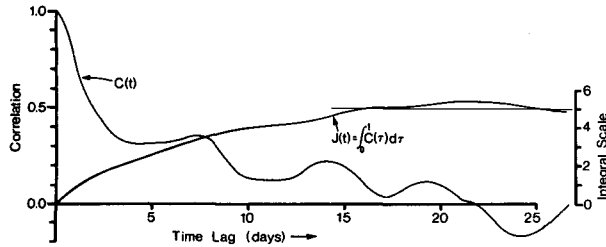


FIG. 6. The autocovariance function $C(t)$ and its integral $J(t)$ for the Eden tide gauge time series. The raw data were filtered to remove tides and other high frequency information and then subsampled at 0.5 day intervals. The function $J(t)$ approaches an asymptote, as t becomes large, which we identify as being close to a period of 5 days.

dict the prediction based on them. How does this discrepancy arise?

Consider the sea level, h_w , at a particular location. It may be decomposed into an isostatic portion, h_i , another signal of interest (e.g., the CTW signal), h_0 , and noise, ϵ_0 , i.e., $h_w = h_i + h_0 + \epsilon_0$. By definition, the isostatic portion, h_i , is proportional to the changing atmospheric pressure, p_a : $h_i = b_0 p_a$, where $b_0 = -0.99 \text{ cm mb}^{-1}$. Then, $h_w = b_0 p_a + h_0 + \epsilon_0$. For the coastal tide gauge stations, h_w was measured directly; for the bottom pressure gauges it was estimated as $(p_b - p_a)$. The linear correlation (r^2) and regression (b) coefficients (Table 1) were calculated between h_w and p_a using the simple regression model, $h_w = a + b p_a + \epsilon_1$. Note that the noise ϵ_1 in this regression equation implicitly includes any signals, h_0 , which are either out of phase or incoherent with the atmospheric pressure. To interpret results from this regression model, we must consider both the correlation and regression coefficients. If r^2 is near 1, then ϵ_1 is small and h_0 is small, i.e., there are no other interesting signals that are out of phase with the pressure; if r^2 is near 1, and $b = -1$, we can infer that CTW signals in the sea level must be small (but note that higher mode CTWs, which have little surface expression, may still be present). This seems to be the case at Hobart, where Hamon found r^2 to be 0.87 and b to be -1.07 ± 0.11 ; even treating these error bars as overly optimistic, we would conclude that at Hobart $r^2 = 1$ and $b = -1$, i.e., that the shelf-wave signal must be weak or absent at Hobart. This result is also supported by the ACE current observations: current fluctuations off Maria Island (Fig. 1), near Hobart, are relatively small compared to those farther north (Fig. 4).

If the correlation coefficient r^2 of the regression model is significantly smaller than one (but still greater than zero), then ϵ_1 is not small and probably includes some interesting signals, h_0 , which may be either incoherent with the atmospheric pressure or simply out of phase with it. If $r^2 < 1$ and $b = -1$, then we have a local isostatic response in the presence of other interesting signals, such as CTWs. This appears to be the case at Eden, where Hamon found $r^2 = 0.26$ and $b = -0.71 \pm 0.23$ in 1957, and $r^2 = 0.56$ and $b = -0.87$

± 0.20 in 1960; ACE results show $r^2 = 0.49$ and $b = -1.29 \pm 0.43$ at the coastal tide gauge, and $r^2 = 0.56$ and $b = -1.03 \pm 0.31$ at mooring 11. Correcting for the over-optimism in Hamon's error bars, we clearly cannot reject the hypothesis that $r^2 < 1$ and $b = -1$ at Eden. Thus, Clarke and Thompson (1984) should not have ruled out the possibility of CTW signals at Eden.

An important part of Hamon's observations dealt with the apparent propagation of phase of the adjusted sea level northwards along the east Australian coast. Using the ACE adjusted sea level ($h = h_w - h_i$) or subsurface pressure data to compute lagged cross-correlation functions, we found that observations at more northerly stations typically lag those at southerly ones. A contour plot (Fig. 7) of the lagged correlations of each station against Eden shows a distinct tendency for phase to propagate northwards. A linear regression of the time lag at the maximum of each cross-correlation function (small squares in Fig. 7) against longshore displacement indicates a "best fit" phase speed of 3.34 m s^{-1} , which is slightly lower than that of Clarke and Thompson. We conclude then that we probably do have CTW-like signals propagating through the ACE area that warrant more detailed analysis.

c. The wind field

Wind measurements with good exposure were available at seven sites: Gabo Island, Green Cape, Montagu Island, Wollongong, Norah Head, Smokey Cape and Coff's Harbour, listed from south to north. The largest

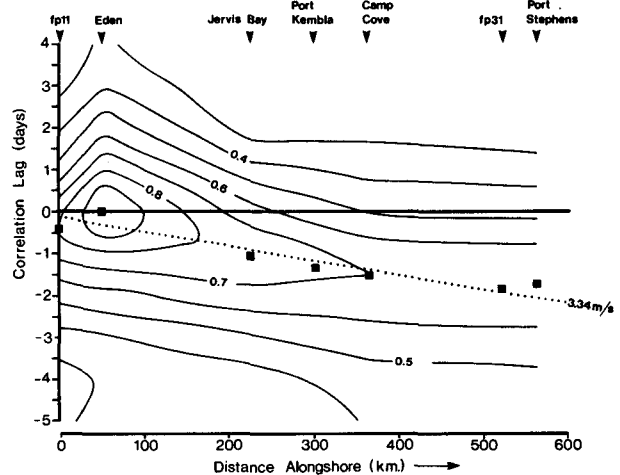


FIG. 7. Contours of equal correlation plotted in a plane of time lag, in days, and distance north of Cape Howe. All time series are correlated against Eden as the reference site. The square symbols indicate the positions for specific displacements of the local maxima in the cross-correlation functions. The dotted line is a least-squares fit through those points indicating the probable northward pattern propagation rate of 3.34 m s^{-1} .

separation between any adjacent pair of these sites was only 250 km (between Norah Head and Smokey Cape). Figure 8 shows a plot of wind stress vectors for the ACE experimental period from three locations in the ACE area. Two important properties of the wind field are apparent from this figure. First, the variance in the wind stress field decays rapidly with distance north from Cape Howe. Second, the variability in wind stresses measured at widely separated positions is very similar. Coherence calculations indicate that though the amplitudes of fluctuations do decay northwards the shape remains remarkably invariant. They also indicate that the phase of the longshore wind stress field propagates northwards nondispersively. Specifically in the range of periods 3 to 20 days the phase difference between Montagu Island and Smokey Cape is 0.69 days (± 0.15) and coherence is well above the 95% confidence interval. The longshore separation of these two stations is about 680 km implying a northward phase speed of 11.4 m s^{-1} . Between Montagu Island and Norah Head the phase difference is 0.38 days (± 0.02) implying (for $x = 350 \text{ km}$) a phase speed of 10.7 m s^{-1} . These values for the wind stress phase speed are very close to the value of 11.5 m s^{-1} used by Clarke and Thompson (1984) in their model of the response of the ACE area.

We conclude, therefore, that the wind systems are propagating phase northwards much more rapidly than oceanographic signals. The wind stress phase speed, about 11 m s^{-1} , is well separated from the speed at which sea-level signals are propagating, about 3.5 m s^{-1} . The properties of the ACE wind field will be discussed at greater length by Forbes (personal communication, 1985).

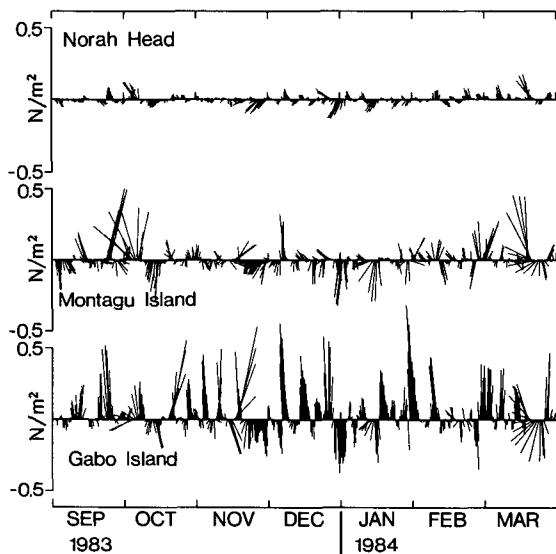


FIG. 8. Wind stress vectors at three coastal stations extending from Gabo Island, near line 1 to Norah Head near line 3. The vectors are rotated so that the principal axis is up and down the diagram. The direction of the principal axis is very nearly in the longshore direction.

d. A transfer function calculation

Contrary to our expectations shelf wave activity is large at the southern end of the experiment. This is consistent with the present observations of sea-level and also with Hamon's observations. The implication is that large amplitude CTWs are entering the southern end of the experimental region and may be propagating through the entire array. Presumably the CTWs experience some modification as they pass through the array, however, we now have to consider the possibility that the free waves may dominate, whereas it was originally expected that the forced waves would dominate. Based on the expectation that the forced waves would dominate, predictions 3 and 4 of Clarke and Thompson (1984) were made. The expected phase speed of $4\text{--}5 \text{ m s}^{-1}$ is based on a particular distribution of amplitude among the dominant modes that need not occur if the dominant waves are not forced locally. The expectation of upward phase propagation at the more northerly lines is similarly the result of analyzing the pure forced problem, as is the prediction that amplitudes should increase northwards. In the total absence of forcing one would expect a slow decline in amplitude due to dissipation by bottom friction or scattering into other wave modes.

Having found that the forced shelf wave seems to be less important than expected, it is appropriate to try to quantify the relative importance of free propagation and forcing. Let us represent the longshore component of current at the northern site then as

$$\hat{V}_n(t) = \sum_{i=0}^N a_i V_s(t - i\Delta t) + \sum_{i=0}^M b_i \tau(t - i\Delta t) \quad (6)$$

where V_n and V_s represent time series of alongshore component of current at the northern and southern sites respectively, the symbol $\hat{}$ represents an estimate, $\tau(t)$ is the wind stress observed at an intermediate location, Δt is the sampling interval (12 hours in all results to be quoted here) and a_i and b_i are weights to be determined. We then constrain the system (6) to find the combination of weights a_i and b_i that represent V_n in the best (least-square sense) way. Various models can be tried by varying the lengths of the filters, i.e., varying N and M above, or by arbitrarily setting one set of weights identically equal to zero and so trying a fit using only the a_i or only the b_i type of weights. The method of solution is simple in principle, but not so in practice. By way of illustration let us consider the simple case of $b_i = 0$ for all i , (the extension including the b_i will be obvious).

Formally the problem reduces to the standard least-squares problem of minimizing E where

$$E = [V_n(t) - \sum_{i=0}^N a_i V_s(t - i\Delta t)]^2 \quad (7)$$

and the overbar indicates an average over time. The solution can be expressed in matrix form:

$$\mathbf{x} = \mathbf{C}\mathbf{y} \quad (8)$$

where the vector $\mathbf{x} = \{x_i\}$ and $\mathbf{y} = \{y_i\}$ and the elements are of the form $x_i = \overline{V_n V_s(t - i\Delta t)}$ and $y_i = a_i$. The matrix \mathbf{C} is a symmetric, positive definite matrix with elements $C_{ij} = \overline{V_s(t - i\Delta t) V_s(t - j\Delta t)}$. Formally we express the solution of this problem as $\mathbf{y} = \mathbf{C}^{-1}\mathbf{x}$. However, the matrix \mathbf{C} generally has a large condition number (ratio of largest to smallest eigenvalue) and so the inverse can be unstable. We proceed, therefore, to solve the problem by singular value decomposition (described in detail in appendix A).

Now let us consider some specific examples of this kind of transfer-function calculation. In the following we will look at the transformation of longshore current components from lines 1 to 2 by representing $V_n(t)$ and $V_s(t)$ in Eq. (6) by f21/125 and f11/125, respectively.

Model 1: Pure current transformation: $N = 5$, $b_i = 0$ for all i . \mathbf{C} is a 6×6 matrix and the solution is stable at \mathbf{y}_4 (see Appendix); the best fit of V_s on V_n accounts for 45.5% of the variance in V_n , i.e., the “predicted” currents correlate with V_n at $r = 0.67$. The weight distribution shows a clear maximum indicating that V_n lags behind V_s . A parabolic fit around the maximum suggests a best estimate of the lag of about 1 day.

Model 2: Pure current transformation: $N = 12$, $b_i = 0$ for all i . \mathbf{C} is a 13×13 matrix and the last stable solution is \mathbf{y}_{10} ; the best fit of V_s on V_n accounts for 51% of the variance, with a correlation coefficient of 0.7. The list of weights extends to greater lags than for model 1 and indicates two peaks at lags of 1.03 and 3.5 days. This suggests that two signals propagate from line 1 to line 2 at speeds of 3.9 and 1.2 m s^{-1} . However, it is interesting to note that increasing the length of the transfer function from six weights to 13 weights results in increasing the amount of variance accounted for in the model by only a few percent. In that sense model 2 seems rather inefficient.

Model 3: Current transformation and winds: $N = M = 5$. This is essentially model 1 modified to include winds. The winds are renormalized so that they have the same variance as the current time series and so that the a_i and b_i all remain dimensionless. \mathbf{C} is a 12×12 matrix and the last stable solution is \mathbf{y}_7 . For this model winds at Montagu Island were used for several reasons: the site is roughly half-way between lines 1 and 2; it is the best exposed of all our wind stations and is likely to be a good representation of the marine wind field; the instrumentation used to record winds was of a relatively high quality. The distribution of weights produced surprising results: the values of a_i were almost exactly the same as in model 1 and accounted for 45.4% of the output variance; the b_i coefficients accounted for only another 4.8% of the output variance. The total

variance accounted for is, of course, larger than that in model 1 because we have increased the information content of the fit, but the increase is not dramatic. We now account for 51.2% of the variance in $V_n(t)$, a larger amount than in models 1 or 2. For this model the best fit to $V_n(t)$ correlates with $V_n(t)$ at $r = 0.70$.

The significant result from these calculations is the clear indication that the CTW signal appears to propagate from line 1 to 2 with little modification by the winds. The addition of winds barely increases our ability to forecast the modification of currents from one line to another. Using variance accounted for as a measure, we are almost 10 times as successful at forecasting the output currents using input currents compared with using winds. We repeated the calculations for model 3 using different wind stations to find which wind station performed best, in the sense of accounting for as much of the total output variance as possible. The best result was obtained from Wollongong (the point on shore closest to line 2) which accounted for 8.6% of the output variance while the a_i terms accounted for 40.1%. Wollongong Head would not be the site of preference for describing the transformation of currents from line 1 to line 2 since it lies very close to line 2; an intermediate site like Montagu Island would be preferred. We conclude then that winds are not of great importance in describing the modification of the currents from one site to another and we should pursue the analysis of the currents into free shelf-wave modes.

4. A modal description of the velocity field

a. The mode shapes

Figure 9 shows a plot of the shapes of the first three CTW eigenfunctions computed separately for the longshore component of velocity at each of the three principal lines of moorings. The eigenfunctions are the solutions $G_n(x, z)$ of Eq. (5), computed simultaneously with the eigenvalues c_n which correspond to the phase speed of each wave. In the long-wave limit the waves are nondispersive and so phase and group velocities are identical. The wave speeds are also entered on Fig. 9. The values of $N^2(z)$ used in Eq. (2) to compute the modes displayed in the figure were calculated from CTD casts along each line of moorings averaged over the entire duration of ACE, i.e., the detailed distribution of $N^2(z)$ varies from one line to another. The bottom topography also varies. These differences do not appear to have a large effect on the structure of the eigenfunctions but do cause significant variation in the wave speeds. (Variation about the mean is about 20%, 13% and 12% for modes 1, 2 and 3, respectively.)

In all nine cases shown in Fig. 9 the largest modal amplitude occurs close inshore and both modes 2 and 3 have nodal lines not far from the shelf edge. Qualitatively the modal shapes are very similar from one line to another. Given these simple observations it is

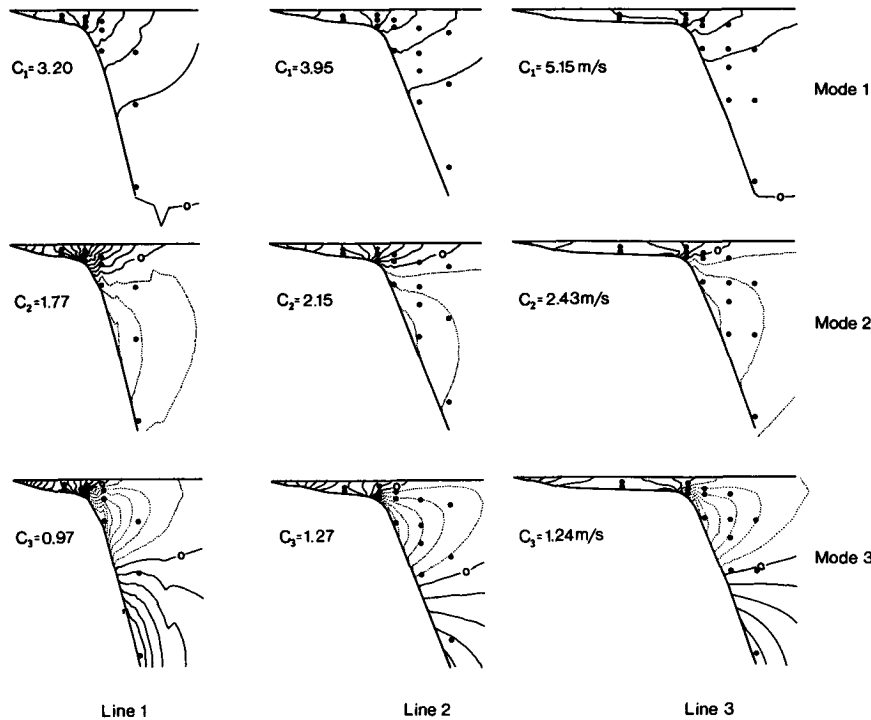


FIG. 9. The first three theoretical CTW mode shapes at each of the 3 principal lines of moorings and the phase speeds associated with each mode. The small dots represent the actual sites where current meter data were acquired on each of the principal lines. The contours are not labeled since the modes can be renormalized without affecting the least-squares computation of modal amplitudes.

difficult to see how any plausible superposition of these modes could yield the variance distributions shown in Fig. 5 which show the largest amplitudes typically at the shelf edge and in some cases seaward of the shelf edge. The conclusion to be drawn is that we are seeing contamination of the shelf-wave signal by the presence of energy from the EAC and its eddy field. Satellite photographs verified that large eddies shed from the current were indeed passing through the ACE region during parts of the experiment. Given the obvious mismatch between the distribution of variance in the experimental array and the shape of the eigenfunctions it is important to examine ways in which the wave field might be decontaminated from the eddy field.

Two methods suggest themselves. The first is to identify periods at each line that are obviously contaminated by eddy activity and excise those parts from the overall record. This approach suffers from a number of problems. It is often not clear when a current meter record is influenced by an EAC eddy; the excising of parts of the data base will inevitably remove part of the CTW signature itself; and the excising operation will inevitably involve some rather subjective judgments. A more objective approach, that removes the eddy activity while leaving the individual time series otherwise intact would be preferred. This turns out to be possible by defining a fourth mode, which we called

an eddy mode, that described the shape of the eddy field.

Examination of detailed EAC events, those that were unambiguously associated with eddies because of the presence of corroborating evidence, clearly showed that these large current events were largely restricted to the continental slope region. In contrast, the CTW modes (Fig. 9) all have their largest signals on the continental shelf. Since current meters fm5/1000 on each line ($m = 1, 2, 3$) contain predominantly eddy signals, we assumed that in any particular line the signal at any current meter that is correlated with the currents at fm5/1000 is the eddy part of the total signal at that site and so could be removed. Let us write the longshore component of velocity at fm5/1000 as $V_e(t)$, i.e., the "eddy" component of velocity at that site. Then along the line m find the value of $a(x, z)$ that minimizes a mean-square error E where

$$E = \overline{[V(x, z, t) - aV_e(t)]^2}$$

and the overbar indicates a time average. The values of $a(x, z)$ define then the shape of an eddy mode. Figure 10 shows a plot of the eddy mode computed along line 3. This was chosen as the best line to define an eddy mode since we had good reason to believe that the eddy field was most intense there, and only at line 3 do we have a substantial quantity of data available at

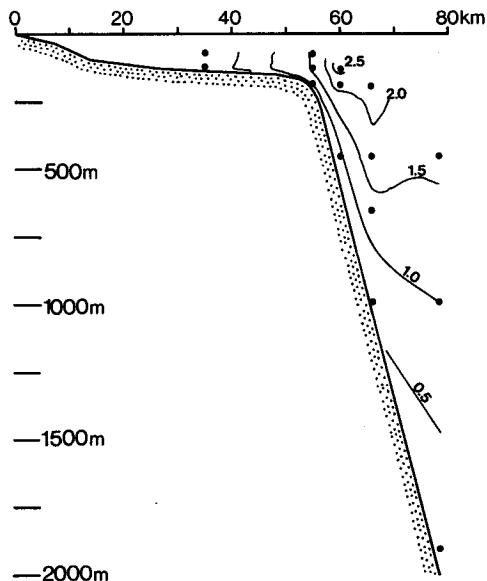


FIG. 10. The "eddy mode" defined as the regression coefficient at each current meter site along line 3 with f35/1000. This mode was used in the subsequent data reduction to absorb signals due to the EAC eddy field.

every site along the line. At both lines 1 and 2, data are missing for almost the entire deployment period at one mooring site each.

The mode shown in Fig. 10 is quite different from the coastal trapped wave modes shown in Fig. 9. In the former the most intense velocities occur seaward of the shelf edge, as one might intuitively expect from an oceanic eddy moving towards the shore. In contrast, at the sites f31/75 and f31/125 the modal amplitudes are extremely small, and this justifies the use of the inshore moorings for exploration for longshore phase propagation. It thus seems reasonable to use the mode shown in Fig. 10 to absorb some of the eddy energy and so optimize our chances of extracting amplitudes of the CTW modes.

b. The modal decomposition

For each mooring line we will expand the observations into three wave modes and one eddy mode. Let $V_j(t)$ be the longshore component of velocity at site (current meter) number j . We break the time series $V_j(t)$ into seven time blocks of 24 days and compute the Fourier transform of the time series for each block. This yields, at each site and for each time block, a series of complex numbers $\hat{V}_j(\omega)$ where ω is 2π divided by T , the period of the Fourier component being examined. For each frequency we define a complex residual \hat{E}_j where:

$$\hat{E}_j = \hat{V}_j - \hat{a}_1 G_{1j} - \hat{a}_2 G_{2j} \cdots - \hat{a}_m G_{mj}$$

and minimize E where

$$E = \sum_{j=1}^N \hat{E}_j \hat{E}_j^*$$

In the above, $m = 4$ is the total number of modes being examined and N is the number of observations \hat{V}_j . The values G_{ij} are the values of the i th velocity mode at instrument number j , and \hat{a}_i is the complex amplitude of the i th mode. Throughout this section any complex number will be indicated by use of the caret symbol, and its complex conjugate will be denoted by an asterisk. The solution for the complex amplitudes is given by the solution of the complex matrix equation:

$$\begin{bmatrix} \sum G_{1j} \hat{V}_j^* \\ \sum G_{2j} \hat{V}_j^* \\ \vdots \\ \sum G_{mj} \hat{V}_j^* \end{bmatrix} = \begin{bmatrix} \sum G_{1j} G_{1j} & \sum G_{1j} G_{2j} & \cdots & \sum G_{1j} G_{mj} \\ \sum G_{2j} G_{1j} & \sum G_{2j} G_{2j} & \cdots & \sum G_{2j} G_{mj} \\ \vdots & \vdots & \ddots & \vdots \\ \sum G_{mj} G_{1j} & \sum G_{mj} G_{2j} & \cdots & \sum G_{mj} G_{mj} \end{bmatrix} \begin{bmatrix} \hat{a}_1^* \\ \hat{a}_2^* \\ \vdots \\ \hat{a}_m^* \end{bmatrix} \quad (9)$$

which we write in the vector form $\hat{\mathbf{b}} = \mathbf{C}\hat{\mathbf{a}}$. As before, the inverse of the real symmetric matrix \mathbf{C} exists, however, the matrix \mathbf{C} is badly conditioned and we chose to extract the solution by singular value decomposition, see appendices A and B. In the following analysis we will use a single set of the CTW eigenfunctions computed for the Stanwell Park line of moorings, line 2, and will use the first three of the dynamical modes. In addition we will use the eddy mode as defined above at line 3 but only after renormalization so that its sum of squares does not dominate over the dynamical modes. A single set of modes is used here since we want, as a first approach at least, to examine the simplest problem of the evolution of the amplitude of a simple set of wave modes in the alongshore direction. We chose line 2 to define the dynamical modes because it is the intermediate site. We chose line 3 to define the eddy mode because we expected it to have the largest amplitude there and, furthermore, only at line 3 do long time series exist at all current meter sites so allowing the mode to be defined at all cross-shelf locations.

c. The dispersion relation

From the four time series determined independently at each of the three lines we can examine one mode at a time and look at the coherence and phase between

any pair of lines. With three lines to analyze we find four different alongshore displacements, specifically these are $\Delta y = 0$ km (for lines 1-1, 2-2 and 3-3) $\Delta y = 160$ km (for lines 2-3) $\Delta y = 360$ km (for lines 1-2) and $\Delta y = 520$ km (for lines 1-3). The phase differences are not all independent, since propagation from line 1 to 2 and from 2 to 3 implies propagation from 1 to 3 provided that the coherences are large. Accepting all of the positive longshore displacements therefore introduces some degree of redundancy among the various phase differences. In order to form an unbiased estimate of longshore propagation rate we decided to include *all* of the redundancy in the system and include estimates of the phase differences for negative displacements. A simple pattern then occurs since a phase difference of $\Delta\theta$ between lines i to j implies $-\Delta\theta$ between lines j to i .

Figure 11 shows the phase differences observed plotted against displacement alongshore for three frequencies and for the three dynamical modes. The points entered with negative displacements are shown with open symbols as these are wholly redundant. For the fourth (eddy) mode few significant coherences were observed, however, when phases were picked off for the fourth mode regardless of the coherence level a random scattering of phases was observed with no obvious sense of organization. At a period of 8 days a tight sequence of phase differences emerges for all possible combinations of lines for mode 1. The phase differences suggest a northward propagation speed of

around 5 m s^{-1} ; the entered value of 4.35 m s^{-1} is derived from the principal axis of the phase differences against displacement. In all other cases, phase speeds indicated on Fig. 11 are derived from a principal axis calculation. Also at 8 days, we see that modes 2 and 3 show a definite tendency for northward phase propagation though the scatter of points about the fitted line is large for mode 2. The fits do indicate that mode 2 propagates slower than mode 1 and that mode 3 propagates slower than mode 2. A striking result of this analysis is that though the speeds for a given mode will be seen to vary quite sharply with frequency in no case do we find that the phase speed for mode 3 exceeds that for mode 2 nor that for mode 2 exceeds the phase speed for mode 1.

At a 6 day period (Fig. 11b) the fastest mode, mode 1, shows a large scatter of phase observations about the fitted line, mode 2 shows a tight collection of points and mode 3 a wide scatter. The phase speeds indicated for modes 2 and 3 are very close and, given the wide scatter in the distribution of points for the mode 3 plot, the difference in phase speed is not significant. That we still observe $C_2 > C_3$ must be considered fortuitous.

For mode 1 at a period of 4 days (Fig. 11a) we see that though coherence was large enough to estimate phase differences between lines 1 and 2 and between lines 1 and 3, it was too low between lines 2 and 3, the closest pair of lines! The coherences corresponding to the other phase estimates for mode 1 are relatively low but do suggest that a propagating signal exists despite

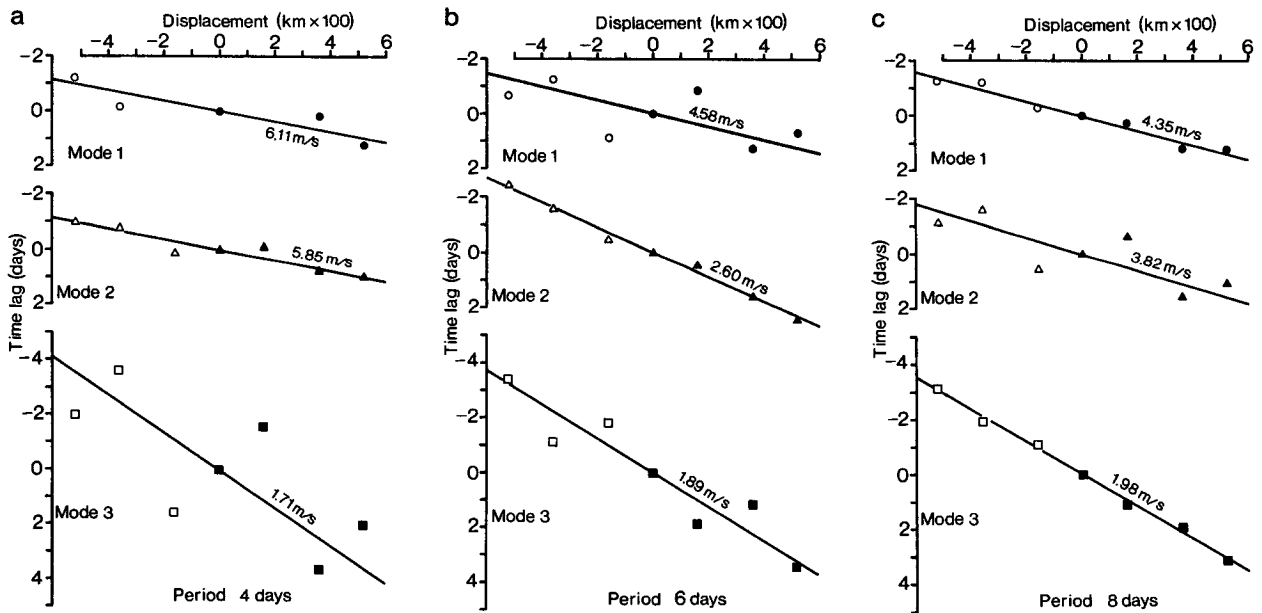


FIG. 11. Phase difference of complex amplitudes for the three dynamical modes at three different frequencies plotted against displacement alongshore. Where an expected entry is missing, the coherence was too low to provide a stable phase estimate. The open symbols represent points that are wholly redundant. The solid symbols carry some degree of redundancy since for large coherences wave propagation from line 1 to 2 and from line 2 to 3 implies propagation from 1 to 3. For small coherence values this is not true and all points with positive displacements become independent. The solid lines indicate the phase speed estimated by the major axis of the principal ellipse through the entered points.

the scatter among the phases. There is rather less scatter in the phase differences for mode 2. Once again mode 2 is slightly, but not significantly, slower than the observed speed for mode 1 and the ordering with $C_1 > C_2$ must be considered fortuitous.

The phase observations are all, of course, cyclic over 360° , or in Fig. 11a, cyclic over a time delay of 4 days and, thus, each phase estimate has an inherent ambiguity of (in the case of Fig. 11a) 4 days. The particular choice of points shown in Fig. 11a was adopted for two reasons. First, we do have physical reasons for expecting northward phase propagation, and second, any other reasonable alternative produces a very wide scatter of phase differences, almost circular, that barely allows a preferred sense of propagation to be estimated. However, for this particular case there is clearly some subjectivity in the interpretation of the phase diagram. The problem of subjectivity gets worse at shorter periods and so we decided that phase diagrams for periods less than 4 days should not be used. The subjectivity problem arose on only two occasions for results that will be quoted here, in both cases for mode 3, at periods of 4 and 4.8 days.

Table 3 shows a list of the observed phase speeds (m s^{-1}) for each of the three dynamical modes. Also listed are the estimated wavenumbers computed as $k_i = \omega/C_i$ where k_i and C_i are the estimated wavenumber and phase speed for mode i . From this table we can produce the dispersion diagrams shown in Figs. 12a, b and c. On Fig. 12 we enter for each mode separately the estimated wavenumber plotted against the frequency of the spectral line under examination. The error bars shown for each point entered represent the frequency bandwidth. The frequencies examined are low enough that the long wave approximation is good; at a period of 4 days $(\omega/f)^2 \approx 0.04$. On each of the plots in Fig. 12 the solid line is the expected dispersion relation based on the long-wave approximation for coastal trapped waves. Specifically, a mean theoretical phase speed has been estimated for the entire ACE array using the phase speeds listed on Fig. 9 and for any individual mode computing the harmonic mean:

TABLE 3. Phase speeds estimated at discrete periods for each of the three wave modes, and the associated wavenumber estimates. The phase speeds were estimated from the direction of the major axis of the principal ellipse of the various phase differences plotted against displacement.

Period (days)	Phase speeds (m s^{-1})			Wave numbers ($\text{m}^{-1} \times 10^5$)		
	C_1	C_2	C_3	k_1	k_2	k_3
24	4.77	2.47	0.96	0.064	0.123	0.316
12	3.30	1.77	1.11	0.184	0.342	0.546
8	4.35	3.82	1.98	0.209	0.238	0.459
6	4.58	2.60	1.89	0.265	0.467	0.641
4.8	10.82	2.33	1.34	0.140	0.651	1.127
4	6.11	5.85	1.71	0.298	0.311	1.065

$$C_i^{-1} = \frac{1}{L} \int_0^L C_i^{-1} dy.$$

The dashed lines show the average dispersion relation defined by the empirical observations. The shaded area on the right hand side of each plot designates an area where the length of the array exceeds the wavelength of any fitted wave. This is effectively (but not quite) a Nyquist wavelength for the array and we cannot reliably estimate any wavenumbers in that region. In fact, as was discussed earlier, some degree of subjectivity arises before we enter that region and the two points at periods of 4 and 4.8 days for mode 3 (Fig. 12c) should be interpreted with some caution.

Figure 12a shows a plot of frequency versus wavenumber for mode 1 at six frequencies. All but one of the points lie above the theoretical long-wave speed of 3.78 m s^{-1} ; an increase in the theoretical wave speed of 1 m s^{-1} would produce a good fit. However, with the exception of one point, at a period of 4.8 days, the experimental dispersion relation is approximately linear as is expected theoretically.

Figure 12b shows the dispersion characteristics for mode 2 at the same six frequencies as in Fig. 12a, and with the exception of a single outlier, the empirical dispersion relation is once again a good approximation of a straight line. Also, as in Fig. 12a, the experimental dispersion points are at systematically higher phase speeds than theory predicts with only one point below the theoretical curve. An increase of only 0.5 m s^{-1} in the theoretical speed would produce good agreement.

Figure 12c shows the same plot for mode 3. Once again the experimental data show a bias towards wave speeds higher than theory predicts. An increase of 0.5 m s^{-1} would, as in Fig. 12b, produce good agreement. The scatter about linearity appears to be rather greater for mode 3 than for the first two modes, but that is probably not an unexpected result. Indeed, in hindsight it seems quite remarkable that we have been able to make a reasonably convincing fit to three wave modes.

Figure 13 displays the variance in each mode plotted against frequency for each of the three principal lines of current meters. We define the variance of mode i as $\sigma_i^2 = \hat{a}_i \hat{a}_i^*$ where \hat{a}_i is the complex amplitude derived from Eq. (9). The variance is averaged over time and defined separately at each line. Since each mode, the three dynamical modes and the empirical eddy mode, is normalized differently, only limited comparisons between modes can be made on this plot. On Fig. 13 we see that the spectra of each mode are generally red, i.e., there is generally more energy at lower frequencies than higher. (Note that these plots are linear in frequency and energy and so are variance conserving plots.) However, at line 1 we see that the spectra peak at a period of 8 days for each of the three dynamical modes. The fourth mode for each line shows the most pronounced red spectra. Rather surprisingly it appears that the second line carries less variance, in the dynamical

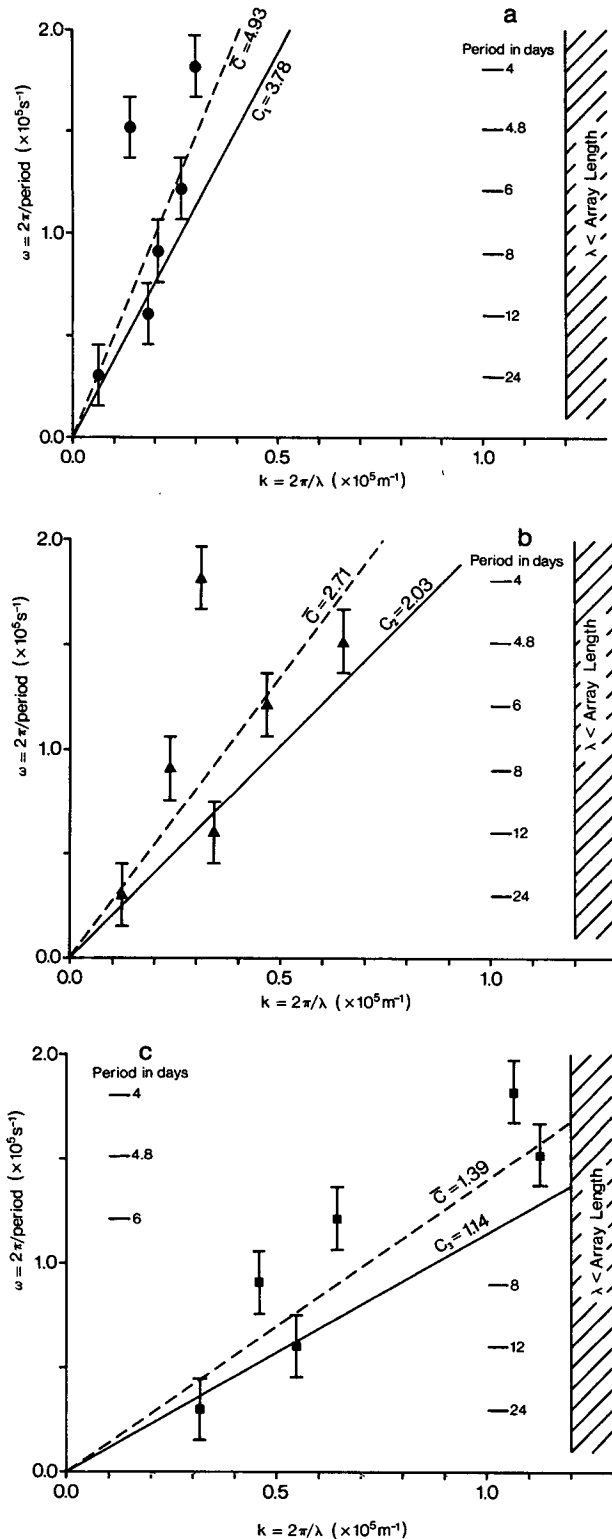


FIG. 12. Empirical dispersion relation for (a) mode 1, (b) mode 2 and (c) mode 3. The bold line shows the expected free wave speed and the dashed line the mean phase speed of the observations, defined as $C = [1/N \sum C_i^{-1}]^{-1}$, i.e., the harmonic mean of the individual phase speed estimates.

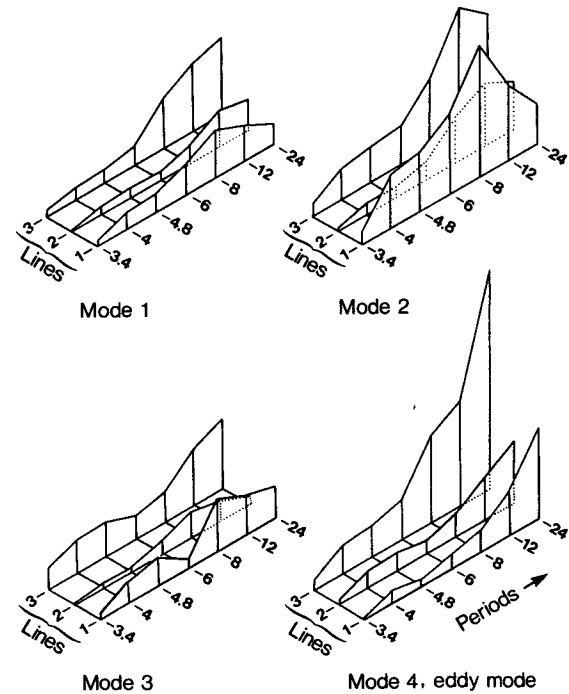


FIG. 13. Energy spectra for each of the modes extracted plotted for comparison between each line.

ical modes, than does line 1, whereas lines 1 and 3 are very similar in their energy levels. Since some moorings on line 3 were damaged by eddies it should come as no surprise to see, in Fig. 13, that the energy levels in mode 4 are very much greater at line 3 than at either of the other two lines.

In summary, Fig. 12 indicates that the dispersion characteristics computed from the ACE moored array are a reasonable approximation to the theoretical dispersion curves for the first three coastal trapped wave modes. In each case the theoretically predicted wave speed is systematically less than the experimentally determined wave speeds by 0.5 to 1 m s⁻¹, or about 25% of the theoretical wave speeds. These results suggest that after the extraneous eddy signal is removed from the data the physics of coastal trapped waves is a good descriptor of the motions on the continental shelf. However, some of the coherences used in constructing the phase plots of Fig. 11, are fairly low, indicating that a simple model of linear phase propagation at a constant speed may not necessarily account for a large fraction of the total variance at any frequency. Furthermore, Fig. 11 also shows a substantial amount of scatter of the time lags about the linear phase propagation speed indicating that still more variance is not accounted for by a simple coastal trapped wave model. In order to explore to what extent the theory of trapped waves can account for the variability observed at any one location a different approach is needed.

d. Analysis in the time domain

The expansion of current observations into modal amplitudes as described in an earlier section can be executed at individual times, rather than for Fourier coefficients, producing explicit time series of amplitudes for each mode. For the three dynamical modes the evolution alongshore can then be compared with the predictions of forced CTW theory. The methods used are described by Clarke and Van Gorder (1986). Since a detailed description of the specific procedures used and the results obtained will be described elsewhere (J. A. Church, 1986), we will restrict ourselves here to an overview of some of the results pertinent to a synthesis of the Australian Coastal Experiment.

We represent pressure as a sum of modes as in Eq. (1) where the functions $F_n(x, z)$ are solutions of an eigenvalue problem, Eq. (2). The amplitudes of the modes are described by a set of forced wave equations that are coupled by frictional coefficients

$$-\frac{1}{c_j} \frac{\partial \phi_j}{\partial t} + \frac{\partial \phi_j}{\partial y} - a_{jj} \phi_j = B_j \tau^y(y, t) + \sum_{\substack{i=1 \\ i \neq j}}^{\infty} a_{ij} \phi_j. \quad (10)$$

As before the longshore velocities are expanded in a series [Eq. (4)] with on-offshore modes related to the eigenfunctions of Eq. (2) by the geostrophic relation, Eq. (5). These equations then can be used (J. A. Church, 1985) to expand the velocities observed at line 1 in the 3 local dynamical and one local eddy mode so producing the amplitudes ϕ_1 , ϕ_2 and ϕ_3 at one value of the alongshore coordinate y , say, at $y = 0$. Equation (10) then can be used to forecast the values of ϕ_1 , ϕ_2 and ϕ_3 at the two northerly lines and compare the predictions with observations.

The eddy mode cannot, of course, be described by Eq. (10), so in making a comparison between the predictions from theory and observations it is important to compare only the inherently predictable parts of the current field. From the observed currents at any particular line we define two new fields that differ slightly from each other. After analysis into the four modes we define the reconstructed currents (V_R) as the sum of the first three (dynamical) modes, i.e., the CTW part of the signal. The de-eddied currents V_d are defined as the observed currents minus the eddy signal. Specifically, at any line we compute ϕ_i by minimizing E where

$$E = [V(x, z, t) - \sum_{i=1}^4 G_i(x, z) \phi_i(t)]^2$$

then

$$\left. \begin{aligned} V_R(x, z, t) &= \sum_{i=1}^3 G_i(x, z) \phi_i(t) \\ V_d(x, z, t) &= V(x, z, t) - G_4(x, z) \phi_4(t) \end{aligned} \right\}$$

These time series are not identical. Both attempt in

some sense to represent the dynamical signal but V_d includes the velocity signal that is not fitted by the least-squares procedure. Over line 1 the gross correlation coefficient between V_d and V_R is about 0.9. This represents how well the least-squares procedure is working. Since the decomposition is good only to a correlation level of about 0.9 we cannot expect a forecast to do as well.

Table 4 summarizes the results of using the modal amplitudes that result from an analysis of line 1 and Eq. (10) to forecast the modal amplitudes at line 2. The "observed variances" are of the reconstructed currents at line 2 (i.e., the CTW part of the current field) and the "predicted variances" result from the modal amplitudes forecast by Eq. (10). The energy levels have been predicted accurately: the predicted and observed variances averaged over line 2 are 36.7 and 41.6 $\text{cm}^2 \text{s}^{-2}$, respectively. These are much closer to each other than to the equivalent figure for line 1, 90.7 $\text{cm}^2 \text{s}^{-2}$.

The correlation coefficients listed in Table 4 indicate that comparison between predicted and observed current fields is significant at high confidence levels. At the inshore sites the correlations are significantly different from zero at the 99.99% confidence level. (As before we assume 1 degree of freedom is accumulated every 5 days.) A stronger null hypothesis would be the equivalent of the meteorological persistence forecast, i.e., that conditions do not change along the shelf. Using the reconstructed velocities, defined earlier, the correlation coefficient between f11/75 and f21/75 is 0.25; the equivalent correlation in Table 4 is 0.62, very much higher. Furthermore, a system with population correlation of 0.25 and 36 degrees of freedom has an upper 95% confidence level of 0.48, less than the 0.62 observed which differs from the population at the 99.8% level.

TABLE 4. Variances at line 2 forecast from an analysis of line 1 and the dynamics of CTWs (the predicted variance); and the reconstructed (observed) variance for comparison. The correlation coefficients between the two fields is also listed. Variances are in $\text{cm}^2 \text{s}^{-2}$.

Meter	Observed variance	Predicted variance	Correlation
f21/75	119.4	100.2	0.62
f21/125	136.6	115.0	0.62
f22/60	67.4	53.9	0.61
f22/110	72.0	56.6	0.61
f22/175	64.3	50.8	0.55
f23/125	37.3	31.1	0.50
f23/190	32.5	30.6	0.36
f23/450	25.5	32.5	0.00
f24/205	13.8	14.6	0.23
f24/465	11.8	14.9	0.01
f24/650	9.4	11.3	0.24
f24/1000	7.4	6.4	0.51
f25/250	7.1	8.3	0.10
f25/800	3.3	3.3	0.42
f25/1700	16.7	21.2	0.07

Earlier in this paper we examined a general relationship between currents separated by distance along-shore and extracted empirical relationships of the form

$$\hat{V}_n(t) = \sum_{i=1}^N a_i V_s(t - i\Delta t) + \sum_{i=1}^M b_i \tau(t - i\Delta t).$$

The best model yielded an estimate \hat{V}_n that correlated with V_n at the level $r = 0.71$.

The linear predictor (6) is essentially the optimal linear predictor and yields an estimate \hat{V}_n that correlates with V_n at $r = 0.71$; it does do better than the dynamical model but not very much better. The optimal predictor must, by definition, perform better than any other linear predictor including a linear dynamical theory but it is satisfying that the dynamical models do almost as well. Finally we note that the dynamical correlation for inshore currents of 0.62 carries 95% bounds of 0.45 and 0.77, and so is not different from the optimal linear estimator at the 95% confidence level.

5. Discussion

In the free wave analysis we have demonstrated that waves pass through the experimental array and exhibit dispersion characteristics that are strongly indicative of coastal trapped waves. One of the more significant observations from this section is that the empirical dispersion relation suggests that the waves propagate rather faster than theory would lead us to expect. The discrepancy is too large, and of the wrong sign, to be accounted for by mean field advection. We suggest that it might be accounted for by contamination of the free wave by the presence of a relatively small forced wave.

Clarke and Thompson (1984) looked at a pure forced wave problem and found the ocean response to wind forcing, for only one mode, to be of the form

$$p(x, y, z, t) = AF_1(x, z) \cos\left[\frac{1}{2}(l + \omega/c_1)y - \omega t\right] \times \sin[(l - \omega/c_1)y/2]. \quad (11)$$

In Eq. (11) $F_1(x, z)$ is the shape of the first CTW mode (pressure field), c_1 is the longshore phase speed and l is the longshore wavenumber of the wind forcing. Thus patterns propagate along the coast at a speed c_{patt} defined by

$$c_{patt} = \frac{\omega}{\frac{1}{2}(l + \omega/c_1)}$$

$$c_{patt}^{-1} = \frac{1}{2}(c_w^{-1} + c_1^{-1}). \quad (12)$$

The pattern speed is the harmonic mean of the free wave speed and the speed of propagation of wind systems in the longshore direction. Since in our case c_w and c_1 are both northwards, at 11 and 3.78 $m\ s^{-1}$, respectively, the pattern speed is greater than, but in the same direction as, the free wave speed.

The forced wave pattern speed computed from (12) is 5.63 $m\ s^{-1}$ and is greater than the free wave speed and greater than the observed pattern speed, see Fig. (12a). Furthermore, we know from the analysis of section (3d) that we are dealing with neither forced nor free waves. In that section we estimated the ratio of velocity variance in the forced wave/variance in the free wave to be about 0.1. This implies a ratio of signal amplitudes of about $\sqrt{0.1} = 0.3$. Thus it seems reasonable to expect that the resulting pattern speed will be intermediate between the free and forced wave speeds, as actually observed.

However, detailed analysis shows a strong dependence on the phase relationship between the free and forced wave components. The actual pattern speed predicted for ACE can even be less than the free wave speed depending on the initial phase difference at line 1. A simple relationship that conforms fairly well to observations can result if the initial phase difference is near zero. Some evidence exists, see later discussion, that a significant part of the free wave energy is generated in Bass Strait, so it may be reasonable to expect the free and forced waves to be almost in phase at Eden.

The analysis of the forced waves in the time domain indicates quite clearly that we do have predictive skill in the sense that we can use the dynamics of forced topographic waves to forecast future conditions some distance along the coastline. However, the amount of variance accounted for in the forecast is not impressive. The correlation coefficients inshore reach highs of 0.62 indicating that we can account for only about 40% of the observed variance with a trapped wave model. Though this does not sound impressive, the best statistical predictor between line 1 and line 2 inshore currents, performs only marginally better and accounts for about 50% of the variance. We conclude that not all of the energy in the weather forcing band is described by coastal trapped waves.

We now turn to the question of the source of the CTW energy observed in ACE. Clarke and Thompson (1984) assumed there would be negligible CTW energy at Cape Howe (line 1) and that wind forcing in the region northward from there would generate CTWs to be observed at lines 2 and 3. As has been pointed out, CTW energy is already large at line 1 and the CTW energy at line 2 is largely the propagation of CTWs northward from Cape Howe as free waves. The expectation of Clarke and Thompson (1984) and the assumption in designing ACE being wrong, we are forced to consider possible sources of the CTW energy at Cape Howe. The bathymetry and meteorological conditions off southern and southeastern Australia allow for several (speculative) possibilities for generating CTWs that are observable at Cape Howe.

One, of course, is that the CTWs have come a very long way. The winds in the Great Australian Bight are strong and the existence of CTWs there has been discussed by Krause and Radok (1976). The possibility

that CTWs could be generated in the Great Australian Bight, travel in the continental-margin waveguide that bends south, and then north, around Tasmania, exists. (This would assume the shallow (<100 m) but wide aperture caused by Bass Strait would not affect the long CTWs and that the wave energy is not dissipated in that distance.) However, this possibility is not supported by the current meter observations. Although there is significant coherence (at the 95% confidence level) between the alongshore component of the current off Maria Island (f02/125) and off Cape Howe (f11/125), the phase difference is negligible. Furthermore, the variance in the coherent band is nearly an order of magnitude less off Maria Island than off Cape Howe. Currents off Maria Island and Cape Howe show some coherence with the Gabo Island wind. All this suggests that forcing of CTWs by winds off southeastern Australia is more plausible than propagation around Tasmania from the Great Australian Bight. We can pursue this possibility by estimating the energy flux at line 1 and comparing it with the rate of working by the Gabo Island wind stress.

Let us first estimate the CTW flux at Cape Howe. The analysis of Clarke and Battisti (1983) shows that the energy flux through a vertical plane perpendicular to the coast is

$$\mathcal{F} = -\frac{\rho_0}{2f} \sum_i \sum_j \overline{\phi_i \phi_j} \int_0^\infty F_i F_j \frac{\partial h}{\partial x} \Big|_{z=-h(x)} dx$$

where the overbar indicates a time average. Using the orthogonality property of the eigenfunctions:

$$\int_0^\infty F_i F_j \frac{\partial h}{\partial x} \Big|_{z=-h(x)} dx = \delta_{ij} \lambda_i,$$

this becomes

$$\mathcal{F} = -\frac{\rho_0}{2f} \sum_i \overline{\phi_i^2} \lambda_i.$$

Using the modal amplitudes calculated for Cape Howe in section 4d, we get

$$\mathcal{F} = 1.8 \times 10^8 \text{ W.}$$

The three dynamical modes used respectively contribute 30.5%, 49% and 20.5% to this total.

We can estimate the energy generated by the wind between the western end of Bass Strait and Cape Howe by following the argument of Gill and Clarke (1974): Bass Strait has an average depth of about 60 m and is about 250 km wide. The barotropic radius of deformation is small ($\sqrt{gh}/-f \approx 260$ km), so the Strait is about one Rossby radius wide. For a Kelvin wave the fraction of the total wave energy between the coastline and 1 Rossby radius is $(1 - e^{-2}) \approx 0.86$. As a first approximation, let us assume that Bass Strait is 410 km long, infinitely wide and of constant depth (60 m), and that no energy enters the western end of Bass Strait.

By an analysis along the lines of Gill and Clarke (1974), it is possible to work out an analytic solution for the wind forced motion and hence estimate an energy flux of

$$\mathcal{F} = 3.0 \times 10^8 \text{ W.}$$

Reducing this by 8% to allow for friction and a further 14% because Bass Strait is not infinitely wide, we can estimate

$$\mathcal{F} = 2.4 \times 10^8 \text{ W.}$$

This is greater than the energy found at Cape Howe and, in view of the high coherence and the small phase lead of the winds at Gabo Island with respect to the currents at Cape Howe, it seems that wind forcing over Bass Strait is a possible source of the energy at Cape Howe.

Could the wind stress over the ocean east of Bass Strait be sufficient to generate CTWs of the magnitude observed? Results to be presented later (J. A. Church et al., personal communication) indicate that a substantial flux of energy is possible. Solving the CTW equation (1) for the 150 km of shelf between the eastern end of Bass Strait and Cape Howe, assuming coupling coefficients appropriate for Cape Howe, and assuming that $\phi_i(t) = 0$, for all i and t , 150 km to the west, the resulting flux at Cape Howe would be

$$\mathcal{F} = 3.4 \times 10^7 \text{ W}$$

with the three dynamical modes contributing, respectively, 46%, 46% and 8% to this total. This flux is about one-fifth of the measured flux at Cape Howe but the correlation between the "predicted" and observed current at the inshore sites is surprisingly high: it is 0.68 at meter f11/125. The correlations drop away very quickly as we move offshore (the predicted currents are much less than the measured currents) but in view of the simplistic approach taken and the short fetch (150 km, compared to the 410 km fetch in the previous estimate), this model does surprisingly well.

In view of these calculations, there would seem to be sufficient sources of energy to the south and west of Cape Howe to explain the observed CTW energy flux off Cape Howe.

Acknowledgments. The participation of R. L. Smith and A. Huyer in ACE was supported by the U.S. Office of Naval Research, and that of A. J. Clarke by the National Science Foundation Grant OCE-8300029.

The participants from North America, A. J. Clarke, H. J. Freeland, A. Huyer and R. L. Smith would like to thank the C.S.I.R.O. for their hospitality during the data analysis phase of the experiment. Finally, we would like to thank Dr. Phyllis Stabeno for helpful discussions and comments on this paper and Netta Delacretaz for her patience while typing the many drafts.

APPENDIX A

Singular Value Decomposition

In several places in this paper it was necessary to solve a least-squares problem, equation (7), for example. Formally, least-squares problems always reduce to the problem of finding a vector \mathbf{y} when a vector \mathbf{x} and a covariance matrix \mathbf{C} are known, and when \mathbf{x} , \mathbf{C} and \mathbf{y} are related by

$$\mathbf{x} = \mathbf{C}\mathbf{y}. \tag{A1}$$

In the transfer function calculations of section (3d) the vector $\mathbf{x} = \{x_i\}$ is of the form $x_i = V_n(t)V_s(t - i\Delta t)$, and $\mathbf{y} = \{y_i\}$ where $y_i = a_i$. The covariance matrix $\mathbf{C} = \{C_{ij}\}$ is of the form $C_{ij} = V_s(t - i\Delta t)V_s(t - j\Delta t)$. Formally we write the solution \mathbf{y} to problem (A1) as $\mathbf{y} = \mathbf{C}^{-1}\mathbf{x}$. However, for the problems of interest in this paper \mathbf{C} generally has a large condition number (ratio of largest to smallest eigenvalue) and so the inverse can be unstable. In such a case the solution \mathbf{y} varies greatly with small variations in the data. We proceed, therefore, to solve the problem by singular value decomposition.

Let the N eigenvalues and eigenvectors of the $N \times N$ matrix \mathbf{C} be λ_i and \mathbf{e}_i , respectively. Since \mathbf{C} is a covariance matrix (i.e., symmetric and having elements satisfying the Schwartz inequality $|C_{ij}^2/(C_{ii}C_{jj})| \leq 1$) the eigenvalues are all real and positive. If N_0 eigenvalues are exactly zero then the rank of \mathbf{C} is $N - N_0$. In practice, since we are dealing with noisy data, any eigenvalue that lies within the sampling noise level is effectively zero.

Let us expand the vectors \mathbf{x} and \mathbf{y} in terms of the eigenvectors, viz,

$$\mathbf{x} = \sum_{i=1}^N \alpha_i \mathbf{e}_i \quad \text{and} \quad \mathbf{y} = \sum_{i=1}^N \beta_i \mathbf{e}_i. \tag{A2}$$

The coefficients α_i are easily determined using the orthogonality property of the eigenvectors

$$\mathbf{x} \cdot \mathbf{e}_j = \sum_{i=1}^N \alpha_i \mathbf{e}_i \cdot \mathbf{e}_j = \alpha_j. \tag{A3}$$

We can then determine the coefficients β_i in terms of the α_i expansion (A2) in Eq. (A1) and remembering that $\mathbf{C}\mathbf{e}_i = \lambda_i \mathbf{e}_i$:

$$\begin{aligned} \mathbf{x} &= \sum_{i=1}^N \alpha_i \mathbf{e}_i = \mathbf{C}\mathbf{y} = \mathbf{C} \sum_{i=1}^N \beta_i \mathbf{e}_i \\ &= \sum_{i=1}^N \beta_i (\mathbf{C}\mathbf{e}_i) = \sum_{i=1}^N \beta_i \lambda_i \mathbf{e}_i. \end{aligned}$$

Hence, we find in general that $\beta_i = \alpha_i/\lambda_i$ and, using (A3) and (A2), express the general solution to (A1) as,

$$\mathbf{y} = \sum_{i=1}^N \left(\frac{\mathbf{x} \cdot \mathbf{e}_i}{\lambda_i} \right) \mathbf{e}_i. \tag{A4}$$

Assuming that the eigenvalues are ordered so that $\lambda_1 > \lambda_2 > \dots > \lambda_N$ let us write an approximate solution \mathbf{y}_R for \mathbf{y} as

$$\mathbf{y}_R = \sum_{i=1}^R \left(\frac{\mathbf{x} \cdot \mathbf{e}_i}{\lambda_i} \right) \mathbf{e}_i$$

where R is an assumed rank of \mathbf{C} , $R \leq N$. Specifically R is chosen so that any eigenvalues that lie within the noise level are neglected.

APPENDIX B

Estimation of Modal Amplitudes

The amplitudes \hat{a} of the three dynamical and one empirical modes discussed in section (4b) are found by the solution of a complex matrix equation (9). The solution is found, as in appendix A, by singular value decomposition of the covariance matrix \mathbf{C} . A complication, however, is that the matrix \mathbf{C} varies from one line to another due to data loss from various instruments at different times. Hence, even on one line the contributions to \mathbf{C} vary with time. The variations in \mathbf{C} are, however, relatively small.

The modal covariance matrix for the nominal distribution of current meters is

$$\mathbf{C} = \begin{bmatrix} 0.273 & -0.294 & -0.138 & 0.402 \\ -0.294 & 0.470 & 0.318 & -0.261 \\ -0.138 & 0.318 & 0.404 & 0.055 \\ 0.402 & -0.261 & 0.055 & 1.000 \end{bmatrix}$$

The eigenvalues of \mathbf{C} are (1.353, 0.707, 0.069 and 0.017) and these eigenvalues contribute, respectively, (63%, 33%, 3.2% and 0.8%) to the trace of \mathbf{C} . As the matrix \mathbf{C} changes slightly, with instrument failure, etc., the eigenvalues take other discrete values near each of the values listed for the nominal array. Since the matrix \mathbf{C} is varied by fairly small amounts, i.e., the sampling array is not changed dramatically, instead of finding four eigenvalues distributed as above, we find four groups of eigenvalues centered near 63%, 33%, etc. We will call these groups type-a, b, c and type-d eigenvalues respectively. The covariance matrix \mathbf{C} changes by sufficiently small amounts that the smallest a-type eigenvalue is never smaller than the largest b-type, and so on; i.e., the four groups are all well separated and do not overlap.

The variance averaged over all current meters deployed throughout the ACE array is $208 \text{ cm}^2 \text{ s}^{-2}$. The resolution of an Aanderaa current meter is about 1.5 cm s^{-1} , and if we use this value as an estimate of the noise level in our current meter array we find the ratio $100\% \times (\text{noise level})^2/\text{mean variance}$ to be about 1%. So with this primitive argument we see that the smallest eigenvalue of the covariance matrix is too small; it lies below the effective noise level of the system, and should be neglected. Specifically then, we will compute the vector $\hat{\mathbf{a}}$ by singular value decomposition [see appendix

A) and reject contributions from any eigenvalue that constitutes less than some critical percentage of the trace of the matrix \mathbf{C} . Hence, from Eq. (9) we can find the set of four modal amplitudes, complex numbers denoting amplitude and phase, for each block of time at one line of moorings and then repeat the expansion at each of the other two lines of moorings. Thus we find four short time series of modal amplitudes (using 24 day long blocks we get seven distinct observations of the modal amplitudes during the ACE period)] at each line, and we can examine the coherences between each line for each mode and search for phase propagation.

First, consider the modal separation for the 3 main lines at a period of 12 days, the second harmonic of the block length of 24 days. The value $E = \sum \hat{E}_j \hat{E}_j^*$ is the so-called reduced variance ($\Delta\sigma^2$) the amount of variance not accounted for by the best modal fit. Let us compute this as a fraction of the signal variance $\sigma_0^2 = \sum \hat{V}_j \hat{V}_j^*$, and average $\Delta\sigma^2$ and σ_0^2 over the seven time blocks and the three lines. We also define the model variance $\sigma_m^2 = \sum \hat{a}_i \hat{a}_i^*$, and average that also over the seven time blocks and three lines. Let us assume that in the process of computing the complex modal amplitudes \hat{a}_i we accept contributions from the covariance matrix \mathbf{C} corresponding to all eigenvalues exceeding a cutoff value λ_0 , and examine the variation

of the normalized residual variance ($\Delta\sigma^2/\sigma_0^2$) and the model variance (σ_m^2/σ_{m0}^2) where $\sigma_{m0}^2 = \sigma_m^2$ at λ_0 . Figure 14 shows a plot of the normalized reduced variance and the model variance as a function of the eigenvalue cutoff λ_0 . Along the abscissa short lines indicate where actual eigenvalues of the slowly varying matrix \mathbf{C} occur. These are, as discussed earlier, separated into four distinct groups. Figure 14 shows that if the cutoff is set at, say, 8% so that contributions from the a-type and b-type eigenvalues are accepted, and none from the c- and d-type, then the best fit modal amplitudes account for all but 26% of the total variance. If we set the cutoff at 1.5%, so that we include contributions from a-, b- and all c-type eigenvalues, then the model fit is improved, but only marginally, accounting for only another 2% of the observed variance. Meanwhile the variance in the best fit modal amplitudes increases by about 10%. If we now set the cutoff at any value less than 0.5%, so that all eigenvalues are used, all but the last 19% of the observed variance is accounted for. This is not a dramatic improvement, and is achieved at the cost of increasing the variance in the modal amplitudes by about a factor of 6. This rapid increase in the variance in the model represents a type of instability as discussed in appendix A. Between cutoff values of 2% and 2.2% there is a substantial drop in the average model variance and an associated sharp rise in the re-

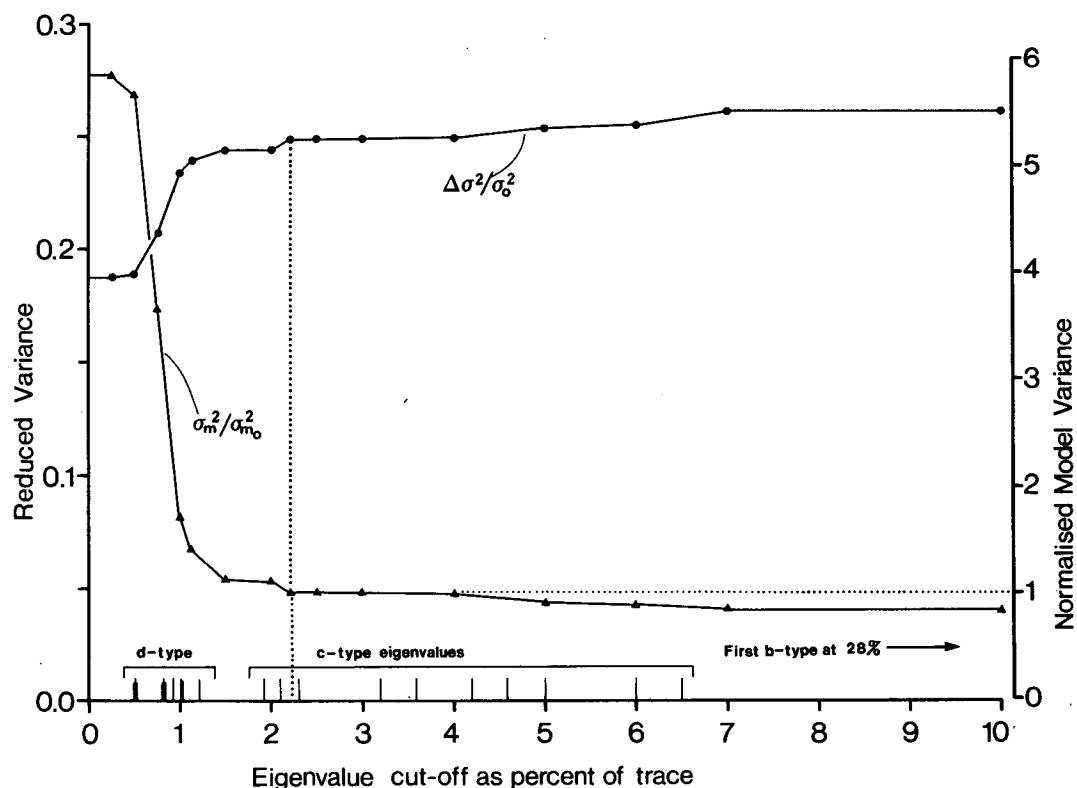


FIG. 14. Response of the least-squares fit model to the inclusion of various eigenvalues in a singular value decomposition.

sidual variance, marked on Fig. 14 by the dotted line. This sharp change occurs as a result of the loss from the array of one instrument on line 2 and affects only one time block. Seen individually it represents a rather severe instability though the averaging involved in Fig. 14 tends to disguise its severity.

Based on the rough guide outlined above, using the noise level of the instruments, we look then to place our eigenvalue cutoff near the boundary between the d- and c-type eigenvalues. The detailed behavior of the model variance and the residual variance plots suggests that the appropriate cutoff value is 2.2% and that value was used in the subsequent analysis.

REFERENCES

- Adams, J. K., and V. T. Buchwald, 1969: The generation of continental shelf waves. *J. Fluid Mech.*, **35**, 815–826.
- Brink, K. H., 1982: The effect of bottom friction on low-frequency coastal trapped waves. *J. Phys. Oceanogr.*, **12**, 127–133.
- , and J. S. Allen, 1978: On the effect of bottom friction on barotropic motion over the continental shelf. *J. Phys. Oceanogr.*, **8**, 919–922.
- Church, J. A., H. J. Freeland and R. L. Smith, 1986: Coastal-trapped waves on the East Australian continental shelf. Part I: Propagation of modes. *J. Phys. Oceanogr.*, **16** (in press).
- Clarke, A. J., 1977: Observations and numerical evidence for wind-forced coastal trapped long waves. *J. Phys. Oceanogr.*, **7**, 231–247.
- , and D. S. Battisti, 1983: Identification of the fortnightly wave observed off the northern coast of the Gulf of Guinea. *J. Phys. Oceanogr.*, **13**, 2192–2200.
- , and R. O. R. Y. Thompson, 1984: Large-scale wind-driven ocean response in the Australian Coastal Experiment region. *J. Phys. Oceanogr.*, **14**, 338–352.
- , and S. Van Gorder, 1986: A method for estimating wind driven shelf and slope water flow. *J. Phys. Oceanogr.*, **16**, 1011–1026.
- Crépon, M., and C. Richez, 1983: Upwellings and Kelvin waves generated by transient atmospheric fronts. *Coastal Oceanography*, H. Gade, A. Edwards and H. Svendsen, Eds., Plenum, 175–203.
- Forbes, A. M. G., 1985: Meteorological data from the Australian Coastal Experiment—A data report. CSIRO Marine Laboratories Rep. No. 170, 1985, Hobart, Tasmania.
- Freeland, H. J., J. A. Church, R. L. Smith and F. M. Boland, 1985: Current meter data from the Australian Coastal Experiment—A data report. CSIRO Marine Laboratories Rep. No. 169, 1985, Hobart, Tasmania.
- Gill, A. E., and A. J. Clarke, 1974: Wind-induced upwelling, coastal currents and sea level changes. *Deep-Sea Res.*, **21**, 325–345.
- , and E. H. Schumann, 1974: The generation of long shelf waves by the wind. *J. Phys. Oceanogr.*, **4**, 83–90.
- Hamon, B. V., 1962: The spectrums of mean sea level at Sydney, Coff's Harbour, and Lord Howe Island. *J. Geophys. Res.*, **67**, 5147–5155. (Correction, 1963. *J. Geophys. Res.*, **68**(15), 4635.)
- , 1966: Continental shelf waves and the effects of atmospheric pressure and wind stress on sea level. *J. Geophys. Res.* **71**, 2883–2893.
- Krause, G., and R. Radok, 1977: Long waves on the southern ocean. *Waves on Water of Variable Depth*, No. 64, *Lecture Notes in Physics*, Australian Academy of Sciences and Springer-Verlag, 235 pp.
- Lumley, J. L., and H. A. Panofsky, 1964: The structure of atmospheric turbulence. Wiley-Interscience, 239 pp.
- Mysak, L. A., 1980: Recent advances in shelf wave dynamics. *Rev. Geophys. Space Phys.*, **18**, 211–241.
- Nilsson, C. S., and G. R. Cresswell, 1981: The formation and evolution of East Australia Current warm core eddies. *Progress in Oceanography*, Vol. 9, Pergamon, 133–183.
- O'Brien, J. J., A. Busalacchi and J. Kindle, 1981: Ocean models of El Niño. *Resource Management and Environmental Uncertainty Lessons from Coastal Upwelling Fisheries*. M. H. Glantz and J. D. Thompson, Eds., Wiley-Interscience, 159–212.
- Robinson, A. R., 1964: Continental shelf waves and the response of the sea level to weather systems. *J. Geophys. Res.*, **69**, 367–368.
- Wells, G., and G. R. Cresswell, 1986: A CSIRO data report on drifting buoys in the ACE period. CSIRO Marine Laboratories Rep. No. 180, 1985, Hobart, Tasmania.